Intermetallics 90 (2017) 63–73

Contents lists available at ScienceDirect

Intermetallics

journal homepage: www.elsevier.com/locate/intermet

Microstructure and oxide particle stability in a novel ODS γ-TiAl alloy processed by spark plasma sintering and laser additive manufacturing

C. Kenel[a,b], K. Dawson[c], J. Barras[d], C. Hauser[d], G. Dasargyri[a], T. Bauer[e], A. Colella[f], A.B. Spierings[e], G.J. Tatlock[c], C. Leinenbach[a,*], K. Wegener[b]

[a] Empa - Swiss Federal Laboratories for Materials Science and Technology, Überlandstrasse 129, 8600, Dübendorf, Switzerland
[b] ETH Zürich, IWF - Institute for Machine Tools and Manufacturing, Leonhardstrasse 21, Zurich, Switzerland
[c] Centre for Materials and Structures, School of Engineering, University of Liverpool, Brownlow Hill, Liverpool, L69 3GH, UK
[d] TWI Technology Centre Yorkshire, Advanced Manufacturing Park, Wallis Way, Catcliffe, Rotherham, S60 5TZ, UK
[e] Inspire AG, icams, Lerchenfeldstrasse 5, St. Gallen, Switzerland
[f] MBN Nanomaterialia S.p.A., Via G. Bortolan 42, 31050, Vascon di Carbonera (TV), Italy

ARTICLE INFO

Keywords:
Gamma-TiAl
Oxide dispersion strengthened
Additive manufacturing
Spark plasma sintering

ABSTRACT

In this work, a novel oxide dispersion strengthened titanium aluminide alloy (Ti-45Al-3Nb- < 0.2Y_2O_3 at.%) was developed for powder-based processing technologies with a focus on spark plasma sintering and additive manufacturing. Titanium aluminides are promising structural intermetallics for weight reduction and an increased performance of high temperature components. The alloy design and selection process was supported by computational thermodynamics based on the CALPHAD approach, taking into account requirements for processing as well as long term alloy behavior under service conditions. Processing trials using spark plasma sintering, direct metal deposition and selective laser melting were conducted to study the alloy behavior, microstructure formation and introduction as well as stability of the ODS particles. Additionally, thermal annealing on the sintered and laser consolidated material was performed. Conventional dual phase α_2-Ti_3Al and γ-TiAl duplex and near-lamellar microstructures were obtained from the processed material. The ODS particles were homogeneously distributed in the alloy matrix after processing in the liquid state. For the direct metal deposition process, the novel alloy was compared to the established GE48-2-2 alloy (Ti-48Al-2Cr-2Nb) in terms of phases, microstructure and texture after processing. A significantly reduced texture formation was observed with the novel alloy. The hardness of the consolidated material shows superior properties for ODS-containing TiAl compared to ODS-free material. This work provides a first step towards tailored alloys for AM and the production of ODS TiAl alloys.

1. Introduction

Titanium aluminides are promising candidates for high temperature capable light-weight materials to increase efficiency and performance in aerospace and automotive applications [1,2]. In recent years, additive manufacturing (AM) has become an interesting alternative to conventional processing like sintering or casting, providing additional geometrical freedom and optimized components with higher complexity, fewer joints and reduced weight. Titanium aluminides are also increasingly processed using powder bed fusion by selective laser melting (SLM) [3–5] and electron beam melting [6–8] as well as directed energy and blown-powder based laser metal deposition (DMD) [5,9,10]. Beside the potentially increased geometrical complexity, AM also allows the production of novel alloys and composites directly in the manufacturing process [9]. The non-equilibrium processing conditions involving high cooling rates create a need for detailed studies in order to develop and select alloys for AM. In this work, the alloy design route is based on previous studies on the influence of cooling rate and composition on the microstructures in rapidly solidified binary Ti-Al and higher-order TiAl alloys [11,12]. Recent *in situ* rapid solidification studies using synchrotron X-ray diffraction could also show the non-equilibrium solidification path in rapidly solidified Ti-48Al [13].

Oxide dispersion strengthened (ODS) alloys have been produced for decades due to their beneficial properties at high temperature as strength retention and creep resistance. Due to particle coarsening, agglomeration and slag-off during casting, powder metallurgical methods, such as sintering, are usually applied for the manufacturing of ODS alloys. Recent studies on Fe-based ODS alloys have proved the

* Corresponding author.
E-mail address: christian.leinenbach@empa.ch (C. Leinenbach).

http://dx.doi.org/10.1016/j.intermet.2017.07.004
Received 4 February 2017; Received in revised form 27 June 2017; Accepted 6 July 2017

possibility to process ODS alloys using liquid state AM technologies and retaining a small dispersoid size by taking advantage of the high solidification and cooling rate inherent to the process [14]. The combination of ODS alloys with AM processing technologies opens a new field for the production of parts with complex shapes, directly from powder. In this work, this approach is expanded to the promising TiAl alloys to produce ODS TiAl alloys by liquid state AM and solid state spark plasma sintering (SPS). This emerging sintering technique has been successfully applied to produce geometrically simple as well as near-net shape parts from titanium aluminides [15,16]. While other aluminide systems have been modified to yield ODS alloys, e.g. ODS FeAl, only a few attempts at ODS TiAl alloys are reported. Er and Gd have been added to the melt to form the corresponding oxides *in situ*, but the particles were not homogeneously distributed [17,18]. Mechanically alloyed Ti-48Al-2Cr-2Nb with Y addition formed Al-Y-O complex oxides after hipping [19]. Grain growth retention up to 1423 K was reported together with no losses in ductility or fracture toughness due to particle formation. To the authors knowledge, no attempts to combine ODS TiAl alloys with AM have been performed so far.

In this work a novel ODS β-solidifying γ-TiAl was studied for powder-based consolidation based on computational thermodynamics and experimental work and taking into account service and processing conditions. The results from consolidation tests by SPS, SLM and DMD are compared in terms of the resulting microstructures, their evolution upon thermal annealing and size of the incorporated dispersoids. Finally, the influence of the processing energy density on dispersoid size and processability of the alloy are discussed. This novel class of material is foreseen to enhance the high temperature capabilities of titanium aluminides by oxide dispersion strengthening combined with geometrical freedom of additive manufacturing.

2. Alloy design and selection

The selection of the alloy serving as matrix for oxide particle strengthening and the second phase itself is dictated by various factors related to service conditions, processing technology and material compatibility. Naturally, a low density and high strength is desired for TiAl alloys to provide high density-normalized specific properties and save weight in structural components. Additional technical requirements in this work were a high chemical homogeneity, a homogeneous distribution of the incorporated oxide particles and microstructural stability at elevated temperatures. From a processing point of view, low anisotropy in as-processed parts is desired and the compatibility of the alloy and the particles for powder-based sintering and AM technologies as SLM and DMD is required. Based on the technical requirements, specific alloy requirements can then be formulated. In modern TiAl alloys enhanced strength is achieved by the stabilization of a higher phase fraction of α_2-Ti_3Al of 20–30% [2,20]. This is typically achieved by a lower Al content of 43–45 at.% compared to earlier Al-rich TiAl alloys, as for example in the Ti-48Al-2Cr-2Nb alloy. Additionally, Nb is commonly added to enhance oxidation resistance and high temperature strength. Regarding the oxidation resistance, the Al content should be maximized at the same time, which is a competing requirement to β-solidification and a high fraction of α_2. So the selected alloy should contain an enhanced fraction of α_2 combined with moderate Nb additions and maximum Al content to ensure oxidation stability under operation conditions. The most beneficial properties in terms of balanced creep resistance, strength and toughness is then typically achieved with lamellar or near-lamellar microstructures consisting of alternating plates of α_2-Ti_3Al and γ-TiAl [1]. Additionally, Ti-Al alloys solidifying solely by the β-phase were found in Ref. [2] to strongly reduce texture and segregation in cast parts. In studies on rapidly solidified binary Ti-Al and ternary Ti-Al-Nb it was found, that these alloys also show strongly reduced segregation behavior under non-equilibrium conditions involving high cooling rates [11,12]. In Al-rich alloys strong segregation of Al was observed, forming a highly Al-enriched liquid

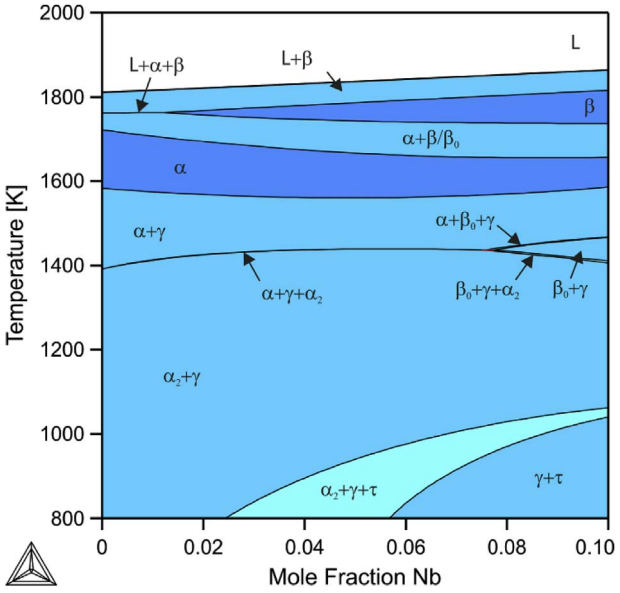

Fig. 1. Calculated isopleth Ti-45Al-(0–10)Nb using a published assessment [22]. Solid single phase (dark), dual phase (intermediate) and triple phase fields (bright) are indicated. The liquid phase field is shown in white. The disordered α-Ti and β-Ti phases, the ordered variants α_2-Ti_3Al and β_0/B2 as well as the γ-TiAl and τ-Ti_4NbAl_3 phases are shown.

towards the final stage of solidification, while Al-lean alloys show only slight changes in Al and Nb content throughout the metastable α_2-rich microstructure. The formation of a supersaturated metastable phase can then later be exploited to produce fine structured material by heat treatments. Based on these findings, the Ti-45Al-xNb system was chosen as a basis for the further alloy selection process.

Supporting thermodynamic calculations were performed based on the CALPHAD approach (CALculation of PHAse Diagrams) using Thermo-Calc 2015a [21] in combination with a published assessment of the Ti-Al-Nb system [22]. Fig. 1 shows a calculated isopleth along Ti-45Al-(0–10)Nb. With increasing Nb additions, the alloy changes from the (quasi-)peritectic solidification type to full β-solidification. At the same time the γ-solvus temperature is slightly decreased and the $\alpha \rightarrow \alpha_2 + \gamma$ decomposition temperature is increased. The former reduces the necessary temperature for solution heat treatments in the α-phase field, while the latter defines the theoretical upper temperature limit of the fully intermetallic structure. At lower temperatures a ternary phase, τ-Ti_4NbAl_3, is predicted to be stable above 2.25 at.% Nb at 800 K. In this work, this phase is considered as an unwanted constituent. However, Nb diffusion is rather slow at low temperatures and thus its formation is expected to be suppressed also at higher Nb content. Under non-equilibrium conditions, extended β-solidification was observed in binary Ti-45Al and ternary Ti-45Al-Nb [12]. For simultaneously Al- and Nb-rich β-solidifying alloys the formation of large amounts of massively transformed γ_m was observed. Consequently, a slight stabilization of the β-phase is sufficient to ensure the desired solidification path. Based on the data in Fig. 2, no substantial changes are achieved in the γ-solvus and $\alpha \rightarrow \alpha_2 + \gamma$ decomposition temperature beyond alloying levels of 3 at.% Nb.

For processing of ODS alloys maintaining a homogeneous particle distribution is crucial. This problem becomes substantial, when the alloy is processed in the liquid state. ODS alloys are generally not processable by casting due to particle agglomeration and coarsening. Consequently, ODS alloys are typically processed in the solid state using powder metallurgical methods such as sintering and extrusion. In AM, the high solidification and cooling rates enable the retention of homogeneously distributed particles in Fe-base alloys [14]. It can be expected, that a strongly segregating Ti-Al alloy may also show local particle trapping in inter-dendritic spaces and agglomeration of

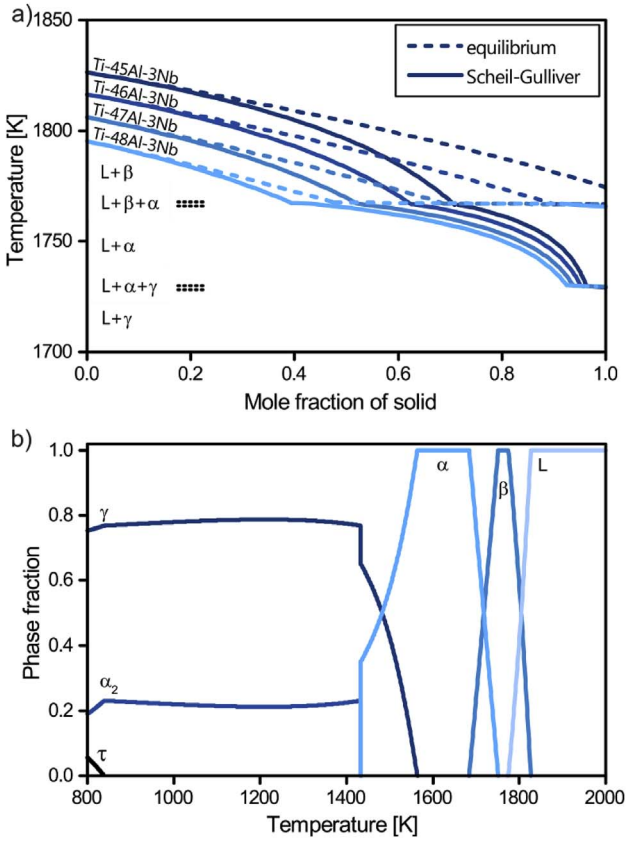

Fig. 2. a) Calculated solidification path of Ti-(45–48)Al-3Nb assuming equilibrium (dashed) and non-equilibrium conditions according to the Scheil-Gulliver model (solid) and b) calculated phase fractions versus temperature for Ti-45Al-3Nb using published data [22]. The stable phases and the fractions of the α, β, α_2, γ and τ phases are indicated.

particles in the remaining melt. If particles are pushed instead of incorporated by the proceeding solidification front, segregation and the formation of a persistent liquid phase prolonging solidification allow for longer time for dispersoid coarsening as well as agglomeration in the inter-dendritic spaces. Additionally, the size of the oxide particles is ideally kept as small as possible to ensure good mechanical and creep properties. This requires a short lifetime of the melt pool, which translates to a low melting range for the chosen alloy. Fig. 3a shows the calculated solidification paths for Ti-(45–48)Al-3Nb for equilibrium and non-equilibrium Scheil-Gulliver conditions. Under equilibrium conditions, only the Ti-45Al-3Nb alloy is expected to solidify solely by the β-phase. Applying the Scheil-Gulliver model, all compositions are predicted to show substantial segregation and final solidification by direct formation of γ from a highly Al-enriched melt. As indicated before, β-solidifying alloys were found to show low segregation under near-equilibrium conditions [23,24] as well as at high cooling rates [12]. Consequently, the effective solidification path follows more closely the equilibrium curve for Ti-45Al-3Nb, while it is better described by the Scheil-Gulliver model for the Al-rich Ti-48Al-3Nb. This discrepancy between the straight-forward application of a simple model and real behavior can be explained by the different diffusivities in the α and β phases. While α has a dense hexagonal close-packed structure, β is body-centered cubic with reduced packing density. Combined with the higher temperature at which β is stable, (back-)diffusion in the β-phase is fast enough to ensure full solidification by β, without the formation of an Al-enriched liquid.

Based on the discussed considerations, Ti-45Al-3Nb was selected as the base alloy for oxide particle incorporation. Fig. 3b shows the calculated phase fractions of the stable phases versus temperature in this alloy. After solidification by β, the alloy crosses the α single phase field before forming γ and finally α_2 and γ become the stable phases. The α_2-fraction is stable above 20% and almost independently from temperature. This ensures additional microstructural stability if components are subjected to varying temperature as both, α_2 and γ, remain stable at the same amount. At low temperatures, a small amount of τ is predicted. However, its solvus temperature is lower than the operation temperature limit and consequently no formation of τ is expected.

3. Experimental

3.1. Powders

Ti-45Al-3Nb and Ti-45Al-3Nb- < $0.2Y_2O_3$ (at.% and mol.%, respectively, for all compositions in this work) intermetallic powders (hereafter named OX 45-3 and OX 45-3 ODS) used for consolidation were produced by mechanical alloying and were supplied by MBN Nanomaterialia S.p.A., Italy. High-energy ball milling (HEBM) of the elemental and oxide powders, as described by Suryanarayana and Froes [18], was performed in equipment made from Ti and under protective atmosphere to avoid contamination in the proprietary Mechanomade® process specifically developed by MBN for the manufacture of TiAl-based ODS material for AM. HEBM was performed with a Ball to Powder Ratio (v/v) 10:1 and with a specific energy of 10.5 kWh/kg. Loading and downloading of the powder from the reactor was made under protective atmosphere (Argon) to prevent oxidation. Other processing details are courtesy of MBN. From the yttria-containing variant, two size fractions with 10–45 μm and 46–106 μm particle size were obtained by sieving (Table 1). From the yttria-free reference alloy only the finer fraction was retrieved for comparative SPS consolidation. The powders produced by HEBM have a globular but irregular shape and a fine structure of typically sub-micrometer thin Nb-rich flakes is visible (Fig. 3a and b). Internal porosity is also observed. For comparative DMD processing trials, a gas-atomized Ti-48Al-2Cr-2Nb (GE48-2-2) powder with a particle size of 46–106 μm was sourced from LPW Technology, UK. This powder is spherical with little internal porosity and has a fine microstructure consisting of equiaxed γ and α_2 lamellae (Fig. 3c).

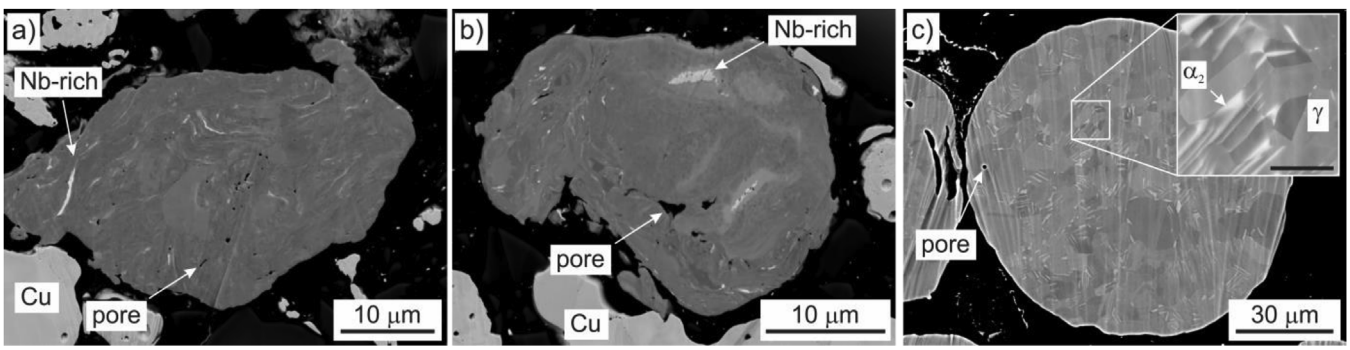

Fig. 3. BSE SEM micrographs of a) OX 45–3, b) OX 45-3 ODS and c) GE48-2-2 (inset: Scale bar is 5 μm). The bright Cu particles in a) and b) are part of the used embedding material.

Table 1
Alloy designation, composition, particle sizes and applied consolidation technology of the studied alloys.

Alloy	Composition (at.%, mol. %)	Particle sizes (μm)	Consolidation
OX 45-3	Ti-45Al-3Nb	10–45	SPS
OX 45-3 ODS	Ti-45Al-3Nb- < $0.2Y_2O_3$	10-45 and 46-106	SPS, SLM, DMD
GE48-2-2	Ti-48Al-2Cr-2Nb	46–106	DMD

3.2. Consolidation

Solid state sintering was performed by SPS on a HP D 10 commercial setup (FCT Systeme GmbH, Germany) in a cylindrical graphite die lined with graphite sheets. Sintering of the 10 mm high billets was performed at a pressure of 50 MPa under vacuum in pulsed current mode with 12 pulses of 3 ms followed by a waiting time of 6 ms with zero current. The heating rate was 100 K/min up to the maximum temperature of 1598 K with a 2 min holding stage before cooling. Heating parameters were adapted from Molénat et al. [15]. In order to compare different laser processing technologies, the area and volume energies E_a and E_v were calculated according to

$$E_a = \frac{P}{v \cdot h}, \quad E_v = \frac{P}{v \cdot h \cdot d} \tag{1}$$

where P is the laser power, v is the scanning speed, h is the hatch distance and d is the layer thickness. SLM was performed on a ConceptLaser M2 (ConceptLaser GmbH, Germany) equipped with a fiber laser operated at 1070 nm in continuous wave mode with a maximum power output of 200 W and a diameter of 100 μm at the focal plane. The powder layer thickness was 50 μm and E_a and E_v were 4.5 J/mm^2 and 90 J/mm^3, respectively. The selected parameters are the result of a study on SLM processing of complex geometries from the OX 45-3 ODS alloy which will be presented in a further paper. The sample geometry is a cuboidal 5 × 5x1.6 mm^3 build consisting of 32 individual layers (see Supplementary Fig. S1a). A unidirectional cross-hatched exposure strategy was applied to ensure a homogeneous energy input. Ar 4.8 was used as processing gas and the oxygen content was controlled to be below 0.1%. DMD was performed using a tri-beam coaxial powder delivery head with a TruDisk 8002 laser source (Trumpf Laser GmbH, Germany) with a maximum power output of 5.3 kW and a spot size of 1.3 mm. For precise movement, the deposition head is mounted on a Reis RV60-40 robot (Reis Robotics, Germany). He was used as transport gas, Ar 4.8 was as applied as shielding gas during processing. The build geometry of OX 45-3 ODS is a cuboid with 20 × 20 × 1.4 mm^3 consisting of 5 layers (Fig. S1b). GE48-2-2 has been deposited as a 14 layer 20 × 15 × 5 mm^3 block (Fig. S1c). For GE48-2-2 the base plate was inductively preheated to 973 K to reduce residual stress formation and cracking. In order to reduce the thermal impact on the dispersoids, the ODS alloy was processed without preheating and at lower energy input. The applied E_a and E_v for OX 45-3 ODS and GE48-2-2 were 120 J/mm^2, 179 J/mm^2 and 444 J/mm^3, 484 J/mm^3, respectively. Both alloys were processed with a bi-directional deposition strategy. The base plates for SLM and DMD were produced from Titanium grade 2.

3.3. Thermal annealing

Short term and high temperature annealing of SPS, SLM and DMD processed specimens were conducted in an induction furnace (in-house developed at Empa, Switzerland) under 5 mbar of Ar 6.0 to avoid excessive elemental losses due to evaporation. The specimen temperature is directly controlled by a ratio pyrometer (QKTR 1085-1, Maurer, ± 1 K). Thermal annealing below 1273 K was performed in a full metal-lined high vacuum furnace (Cambridge, UK) at pressures < 10^{-5} mbar. The specimen temperature was controlled by calibrated thermocouples placed next to the specimen.

3.4. Characterization

For the microstructural analysis the specimens were embedded into epoxy resin and polished using diamond suspensions from 9 to 1 μm. The final polishing step was performed using a non-crystallizing silica solution (20 nm) with H_2O_2 addition. To remove the remaining surface deformation layer present after the final polishing step, Ar ion beam polishing was applied using a Hitachi IM4000 ion beam polisher at 4 kV acceleration voltage and an incident beam angle of 80° to the surface normal direction. After surface preparation, the specimens were investigated using scanning electron microscopy using a Hitachi S3700N equipped with BSE and EDX detectors (EDAX) for imaging and a Hitachi S4800 for high resolution imaging and particle measurements in SLM and DMD processed specimens.

On selected specimens X-ray diffraction (XRD) and XRD pole figure measurements were performed with Cu Kα radiation using a Bruker D8 DISCOVER equipped with a LynxEye 1D detector. The measurement conditions were 40 kV and 40 mA with a step size of 0.02° (2Θ). XRD pole figure data was corrected for defocusing effects and normalized to yield multiples of random distribution (m.r.d.) using the MULTEX software package of Bruker. Additional pinhole snouts were used to restrict the beam diameter to the area of the specimens.

Solid state SPS sintered material was analyzed using transmission electron microscopy (TEM) and scanning transmission electron microscopy (STEM) on an aberration-corrected JEOL 2100FCs S/TEM operating at 200 kV. The electron-transparent lamellas were prepared using a FEI Helios 600i dual beam focused ion beam (FIB) instrument. Specimens were prepared by the lift out method and low energy (2 kV) polishing was applied as final step.

The size of the lamellar colonies and γ-TiAl grains in SPS sintered and heat treated material was determined using the line intersection method on 2560 × 1920 pixel BSE SEM micrographs recorded at 2000× magnification along a rectangular line grid. The fraction of lamellar colonies was determined by their area fraction on the same micrographs. The size distribution of the ODS particles in SPS material was measured on 1024 × 1024 pixel bright-field STEM micrographs at 20′000× magnification using the maximum particle diameter (n_{SPS} = 1718). The fewer and larger ODS particles after SLM and DMD processing were measured on a series of high-resolution SEM micrographs at up to 4096 × 3200 pixels and 32′000× magnification (n_{SLM} = 386 and n_{DMD} = 391). Particle densities were estimated from the same micrographs assuming particle detection in a 2D plane yielding the area number density N/A with N the number of particles and A the area. The volume particle density is then calculated as

$$\frac{N}{V} = \left(\frac{N}{A}\right)^{\frac{3}{2}} \tag{2}$$

with V being the volume. The mean particle center distance l_c can then be estimated as

$$l_c = \left(\frac{3 \cdot V}{4 \cdot \pi \cdot N}\right)^{\frac{1}{3}} \tag{3}$$

assuming a spherical volume element centered at the particle position. Using the median size of the particles d_{median} the inter-particle distance l can be calculated simply as

$$l = l_c - d_{median} \tag{4}$$

For TEM lamellae with a certain thickness, the particle volume density is clearly overestimated by Equation (2). However, the error of this estimation can be neglected in this case where the order-of-magnitude differences in between the different consolidation methods are of interest.

The fraction of retained dispersoids f is calculated using the determined median dispersoid size and volume number densities according to

$$f = \frac{N}{V} \cdot \frac{4 \cdot \pi}{3} \cdot \left(\frac{d_{median}}{2} \right)^3 \quad (5)$$

Vickers hardness (HV) was measured using a Fischerscope HM2000 (Fischer, Germany) on polished specimens prepared for microscopic investigation. The indentation with the Vickers diamond tip was performed with a maximum load of 400 mN and a load increase time of 20 s. For bulk material a minimum of 25 indentations with a spacing larger than 50 μm were measured to ensure statistical relevance of the data. For SPS specimens the hardness was measured perpendicular to the pressing direction, for SLM and DMD the measurements were performed on the z-y plane where z is the build direction. The machine is calibrated using standards to ensure data repeatability and create the necessary correction functions. The typical indentation diameter is in the order of 10 μm.

4. Processing results and discussion

In this section the results from solid and liquid state powder processing are shown. Sintered material was used to study the formed microstructure and its stability upon high temperature annealing. SLM and DMD were applied to test the alloy behavior under AM processing conditions and evaluate microstructure formation, texture and the possibility to achieve a desired microstructure by thermal annealing. Additional TEM investigations provide information about the size and distribution of the oxide particles in the alloy matrix. Finally, the particle incorporation is compared for solid state SPS and liquid state additive SLM and DMD.

4.1. Spark plasma sintering

Solid state consolidation using SPS was successful in producing dense material from the OX 45-3 ODS powder. Fig. 4a shows the fine grained duplex microstructure consisting of lamellar colonies and equiaxed γ and α_2 grains in the as SPS state. After the SPS consolidation, the specimen cools down with a maximum cooling rate of 9 K s^{-1}. Consequently, the specimen contains a high fraction of α_2 phase around 49% and is in a metastable state. For any application, the microstructure needs to be stabilized closer to its equilibrium state. Additionally, fast non-homogeneous cooling gives rise to residual stresses in the as SPS consolidated material. To achieve the stabilization a thermal annealing at 1123 K for 12 h in vacuum was performed. Fig. 4b shows the resulting structure with γ and α_2 fractions of around 75% and 25%, respectively, and a lamellar fraction of 26%. Comparing these results to the calculated phase fractions shown in Fig. 3b, the obtained state is close to equilibrium. Note that the consolidation by SPS was performed at 1598 K, which is in the α phase field for the chosen alloy. So already during consolidation, the formation of a coarse grained lamellar microstructure would be expected. Conventional heat treatments to obtain lamellar microstructures for TiAl alloys typically involve a high temperature treatment in or close to the α phase field at temperatures around 1573 K–1673 K, depending on the composition. Fig. 4c and d shows the resulting microstructures after two step thermal annealing involving a high temperature step at 1573 K or 1673 K for 15 min and the stabilization treatment described before. The two temperatures were selected based on the calculated phase fractions and are close to the lower and upper boundary of the calculated α phase field for this alloy (1563 K–1683 K). The obtained microstructures are very similar to the one obtained by the stabilization annealing only. The measured intersection length of the equiaxed γ grains was determined as 1.4 ± 0.8 μm for the stabilized state and 1.5 ± 1 μm and 1.3 ± 0.6 μm after the thermal annealing at 1573 K and 1673 K, respectively. The fraction of lamellar grains increased from 26% to 36%

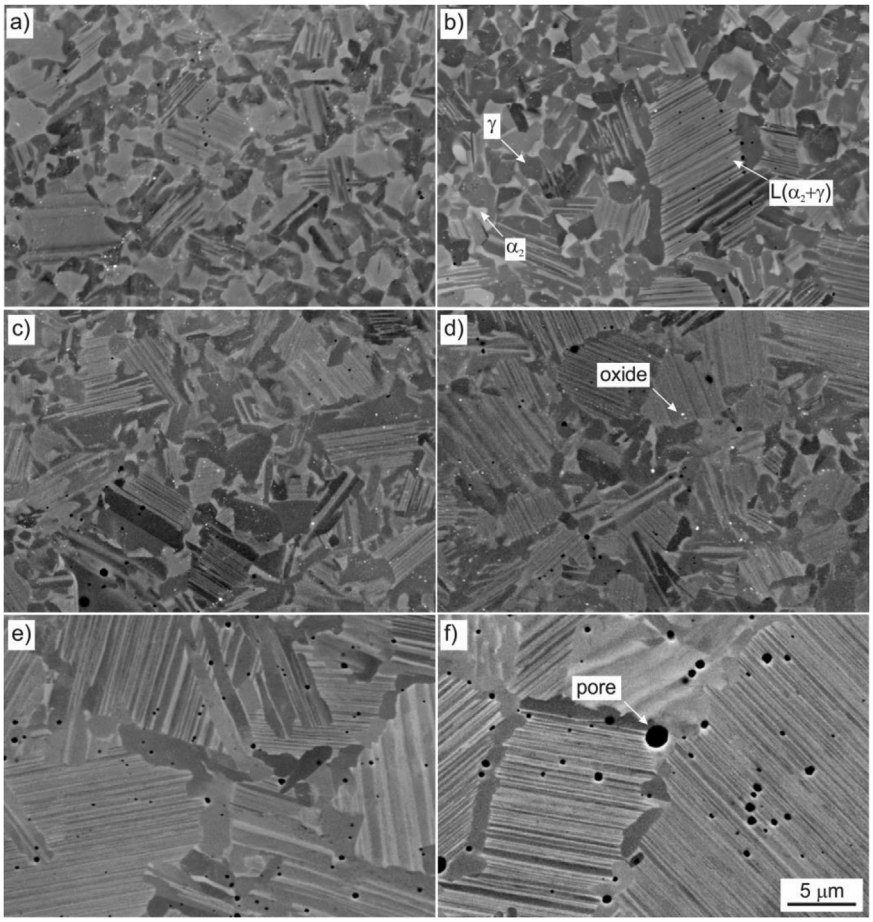

Fig. 4. BSE SEM micrographs of SPS (a–d) OX 45-3 ODS and (e, f) ODS-free OX 45-3 a) in the as SPS state, and after thermal annealing of (b, e) 1123 K/12 h, c) 1573 K/15 min + 1123 K/12 h and (d, f) 1673 K/15 min + 1123 K/12 h. The α_2 (light grey) and γ (dark grey) phases, pores (black) and Y-based oxides (white) are indicated as well as the lamellar colonies formed of $\gamma + \alpha_2$, The scale bar in f) applies for all micrographs.

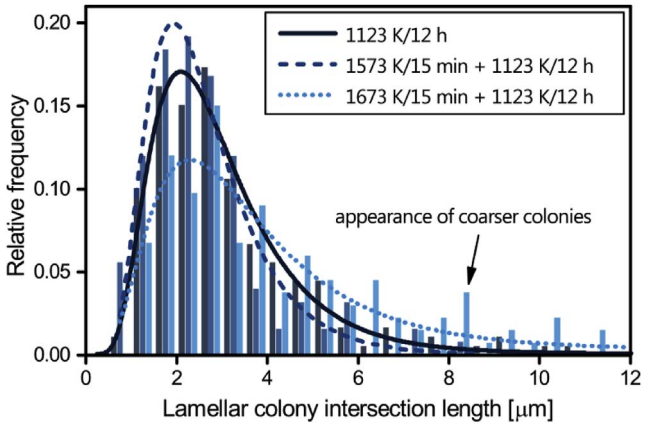

Fig. 5. Distribution of the measured intersection length of lamellar colonies in SPS OX 45-3 ODS after different thermal annealing. Least-square-fitted log-normal distribution curves are shown overlaid.

after 1573 K and to 63% after 1673 K. Fig. 5 shows the distribution of the measured intersection lengths of lamellar colonies after the various thermal annealings for OX 45-3 ODS. Independently from the chosen thermal annealing, the peak values are obtained around 2 μm due to the presence of very small colonies. The mean intersection lengths of lamellar colonies for thermal annealing at 1123 K for 12 h, 1573 K or 1673 K for 15min and the stabilization treatment are 3.2 ± 2.2 μm, 2.6 ± 1.4 μm and 4.4 ± 3.1 μm, respectively. After 1673 K for 15 min the fraction of larger colonies starts to increase, which is also evident from Fig. 4d. At this temperature, the γ grains are slowly dissolving in the disordered α matrix resulting in larger lamellar colonies in the final microstructure. With increasing temperature this process is expected to occur faster as it is observed in the SPS material. Fig. 4e shows the microstructure of the OSD-free variant OX 45-3 after SPS and 1123 K for 12 h. Large lamellar colonies are formed with γ at the colony boundaries along with a multitude of sub-micrometer pores. After a high temperature anneal at 1673 K for 15 min and the stabilization treatment, the microstructure is further coarsened. The mean intersection length of the lamellar colonies after 1123 K for 12 h and 1673 K for 15min plus 1123 K for 12 h are 10.9 ± 8.9 μm and 11.0 ± 8.2 μm, respectively. After high temperature annealing, larger pores appear in the γ-seams along the colony boundaries (Fig. 4f). This pore expansion is explained by a combination of high temperature, absence of strengthening particles and a high internal pressure in the pores. During SPS the pores and any contained gas are compressed with 50 MPa. This is equivalent to an overpressure of 500 bar inside the pores assuming residual gas pores with atmospheric pressure contained in the powder. As the alloy is later annealed, the high internal pressure leads to deformation of the surrounding matrix and an increased pore size. The appearance of the largest pores in the γ-seams further strengthens this argument, as the lamellar structure is expected to have superior creep resistance compared to the γ-phase. Additionally, dissolved gas may be liberated and further contribute to pore expansion. It has to be noted, that the observed pore size is expected to be an overestimate of the true pore size, as chemo-mechanical final polishing is applied. Thus the material is attacked and exposed pores are expected to increase in size.

The observed behavior upon consolidation and thermal annealing shows an exceptional microstructural stability of the produced SPS ODS alloy variant at high temperatures during consolidation and following thermal annealing. The increased microstructural stability of the SPS material can be directly related to the presence of the ODS particles in the alloy matrix. With the possibility to produce near-net shape turbine blades by SPS the newly developed OX 45-3 ODS alloy or similar ODS TiAl alloys have potential applications as solid state sintered component in high temperature environments in the future. Additionally, microstructural stability is a crucial factor for application of SPS consolidated alloys [16]. The introduction of dispersoids effectively limits colony coarsening and allows production of alloy with colony sizes around 5–10 μm promising interesting mechanical properties at high temperatures.

4.2. Selective laser melting

Liquid state consolidation using SLM was successful in creating test parts with low porosity (Fig. 6). Fig. 6a shows the observed microstructure in the as-processed state. In the as-processed state, the major constituent is a metastable α_2 phase which forms during rapid cooling [12]. Starting from the melt pool boundary, a grain selection process takes place producing a gradient in grain size. Subsequent laser scans partly re-melt the previously deposited material and eliminate the very coarse grains. Again, selected grains continue to grow. Consequently, the deposited material contains fine grained former melt pool boundaries and coarser bulk regions. In the material close to the former melt pool boundary a fine structure is visible originating from the primary β cells later transformed to α are visible. Residual porosity below 5 μm is also observed. Based on the spherical shape it is proposed, that these are caused by the entrapped gas from powder production or processing. Material from the same specimen was subjected to a thermal annealing at 1123 K for 12 h similar to the SPS consolidated material. Fig. 6b shows the obtained near-lamellar microstructure consisting of lamellar $\gamma+\alpha_2$ colonies in a size range of 5–30 μm and sub-micrometer γ and α_2 grains formed at the colony boundaries. These grains show an elongated shape and are oriented typically parallel with respect to each other and to one of the adjacent colonies (inset Fig. 6b). This bimodal lamellar structure, fine inside the colonies and coarse at the boundary in between, can be explained by the kinetics of the phase transformation. First, fast decomposition of the former α grains into primary $\gamma+\alpha_2$ colonies takes place upon thermal annealing. The size and shape of the primary lamellar colonies is similar to the α_2-grains observed in the as processed material. This indicates a direct decomposition of the metastable microstructure upon thermal annealing. Later a slow decomposition of the fine structure into a coarser lamellar structure by discontinuous coarsening starts. This requires diffusion over greater length. At 1123 K the diffusion in TiAl alloys is expected to be rather slow based on their intermetallic ordered structure. Consequently, this second transformation is observed in its initial stage after the thermal annealing. Inside the colonies finely distributed dispersoids are visible

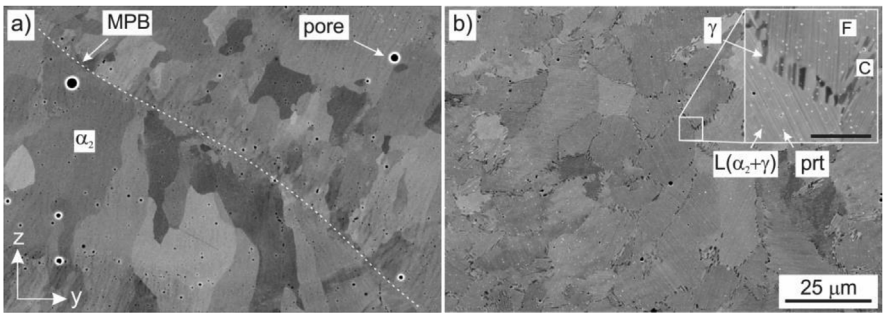

Fig. 6. BSE SEM micrographs of SLM processed OX 45-3 ODS (E_a = 4.5 J/mm^2) in a) as processed state and b) after thermal annealing at 1123 K for 12 h (inset: scale bar = 4 μm). The observed phases, pores, melt pool boundary (MPB), coarse (C) and fine lamellar (F) regions and dispersoids (prt) are indicated. The scale bar in b) applies for both micrographs. The build direction (z) and the beam translation (y) are shown. The scanning direction (x) is out-of-plane.

as bright spots due to the mass contrast of the yttrium-based oxides (inset Fig. 6b). It needs to be pointed out, that the applied thermal annealing temperature is far below conventional heat treatment temperatures to obtain near-lamellar microstructures. In cast parts of similar composition, temperatures as high as 1653 K in the α-field are applied [23]. This is more than 500 K higher than the thermal annealing which was applied in this work. The formation of a supersaturated metastable microstructure during rapid solidification enables such low heat treatment temperatures and phase decomposition.

The obtained results clearly show that the OX 45-3 ODS alloy can be consolidated using laser processing and be transformed into conventional microstructures afterwards. This opens the space to complex shaped ODS TiAl alloys for highly loaded applications. Detailed studies on suitable processing parameter windows and part integrity are needed in the future to enable the application ODS TiAl alloys.

4.3. Direct metal deposition

Compared to the powder-bed based SLM technique, blown-powder based DMD provides higher deposition rates at higher energy densities. In this work, the applied area energy densities for DMD were a factor of 27 higher than for SLM. Fig. 7 shows the observed microstructures for OX 45-3 ODS and GE48-2-2 in the as-processed and annealed state. The Al-rich GE48-2-2 forms a dendritic microstructure consisting of lamellar $\gamma + \alpha_2$ colonies and inter-dendritic γ phase. The Al-leaner OX 45-3 ODS forms a columnar grained structure consisting mainly of the α_2 phase with some spurious γ. The largest dispersoids are visible as white spots in the SEM micrograph. After a thermal annealing at 1123 K for 12 h both alloys start to recrystallize (Fig. 7c and d). While GE48-2-2 retains

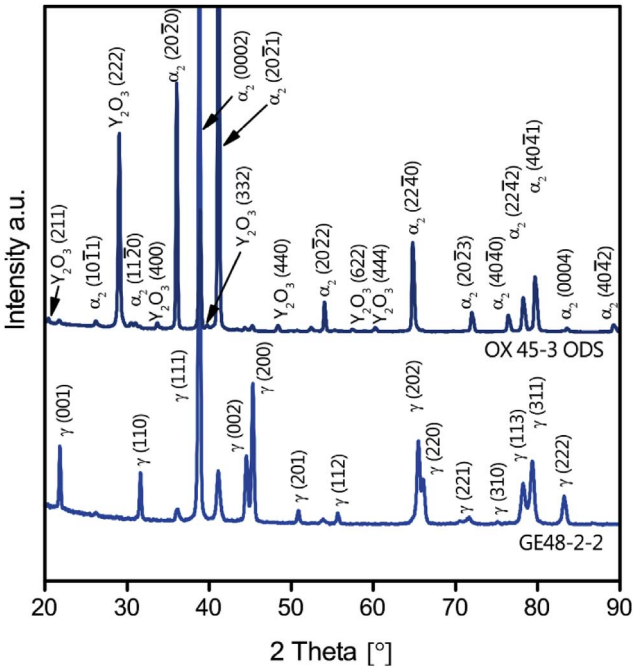

Fig. 8. XRD spectra of DMD processed OX 45-3 ODS (top) and GE48-2-2 (bottom). Peaks of the intermetallic α_2 and γ phases and of Y_2O_3 are indicated.

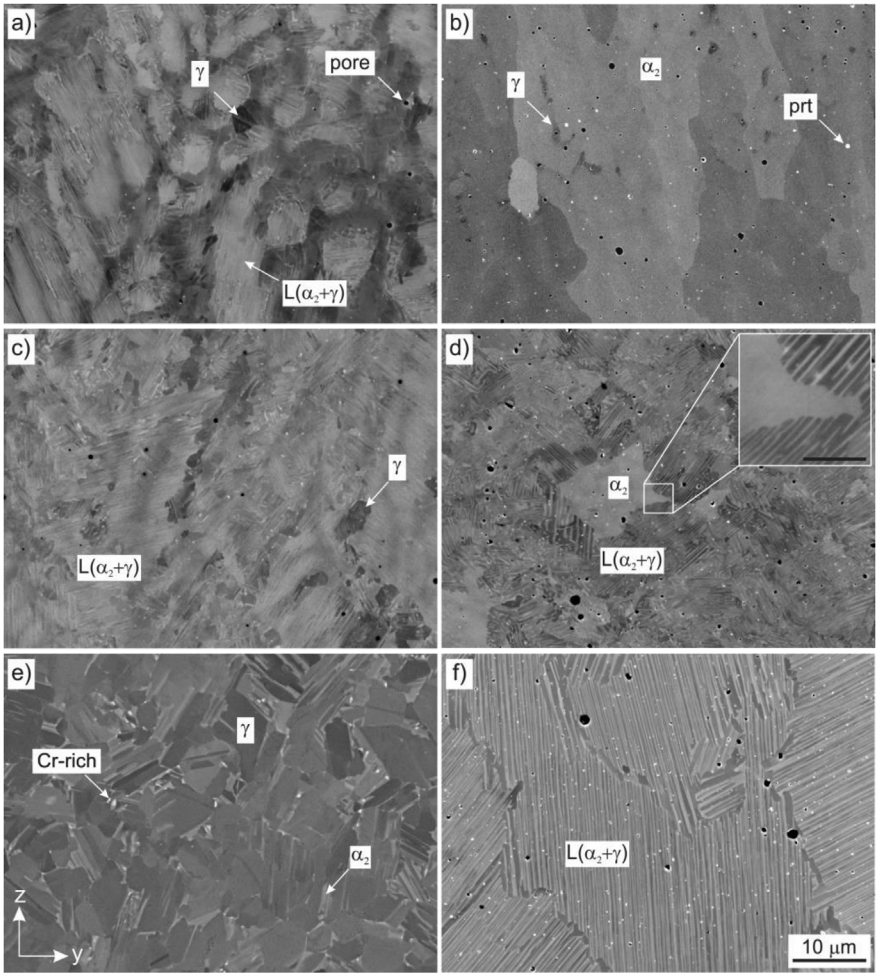

Fig. 7. BSE SEM micrographs of DMD processed a, c, e) GE48-2-2 (E_a = 179 J/mm^2) and b, d, f) OX 45-3 ODS (E_a = 120 J/mm^2). (a, b) in the as processed state and after thermal annealing of (c, d) 1123 K/12 h and (e, f) 1573 K/15 min + 1123 K/12 h. The α_2 and γ phase, pores and dispersoids (prt) are indicated. Bright spots in e) correspond to Cr-rich areas. The scale bar in f) applies for all micrographs (inset: scale bar = 2 µm). The build direction (z) and the beam translation (y) are shown. The scanning direction (x) is out-of-plane.

its fine lamellar structure with equiaxed γ, OX 45-3 ODS decomposes into small lamellar γ + α_2 colonies. Residual areas between the colonies still resemble the α_2 structure observed in the as processed state. The presence of a dual phase structure in these areas with a very fine lamellar spacing would be expected based on the results of annealed SLM-consolidated material (Fig. 6b). If present, the resolution of the SEM or compositional difference and thus contrast was not high enough to resolve this structure. After annealing at 1573 K for 15 min and 1123 K for 12 h, GE48-2-2 is fully transformed into a duplex structure with an increased amount of γ. This is in agreement with established phase diagram data on Ti-48Al-2Cr-2Nb predicting 1573 K to be in the α + γ two phase field and consistent with observations on DMD of similar alloys [5]. OX 45-3 ODS forms a fully lamellar microstructure with ragged colony boundaries, as the chosen temperature is in the α single phase field. Fig. 8 shows XRD spectra of DMD processed OX 45-3 ODS (top) and GE48-2-2 (bottom). The ODS alloy contains a large fraction of α_2 with a minor γ content. Additionally, Y_2O_3 is clearly observed which is enriched at the surface due to partial slagging-off of the oxide particles in the last deposited layer during processing. The GE48-2-2 alloy contains mainly γ together with α_2 based on the relative intensities of the γ(111) and α_2 (20$\bar{2}$1) peaks. This different behavior is explained by the dependence of the solidification path on alloy composition. OX 45-3 ODS is fully β-solidifying, while GE48-2-2 is forming primary β, undergoes a peritectic reaction and then solidifies by α under equilibrium conditions. Recent *in situ* XRD experiments on Ti-48Al at high cooling rates by Ref. [13] show that the formation of β-phase is suppressed at high cooling rates and the alloy forms primary α phase. Additionally, it is presented in Ref. [11] that Al-rich alloys typically show much stronger segregation than Al-lean alloys. Consequently, GE48-2-2 shows a fine structure dominated by the solidification of the α phase, whereas OX 45-3 ODS shows a coarse structure originating from the primary β phase. Beside the phase fractions and segregation, the texture is also strongly influenced by the alloy composition. Fig. 9 shows XRD pole figures for DMD processed GE48-2-2 (top) and OX 45-3 ODS (bottom) for the γ(111)/α_2(0002) reflection (left) and the α_2 (20$\bar{2}$1) reflection (right). For GE48-2-2 a fiber texture is observed for both reflections while OX 45-3 ODS is much less textured based on the intensity distributions. No distinct alignment of the principal peaks of α_2 and γ was observed with the out-of-plane direction in the center of the pole figures. Based on the observed intensity distributions, γ(111)/α_2(0002) is slightly oriented towards the in-plane direction, whereas α_2(20$\bar{2}$1) is observed more frequently at lower angles to the surface normal direction. The distinct ring shape for the α_2(20$\bar{2}$1) pole figure of GE48-2-2 is formed by the other planes of the α_2{20$\bar{2}$1} family of planes rotated around the out-of-plane direction. The calculated ideal inter-planar angles between α_2(20$\bar{2}$1) and α_2(20$\bar{2}$1) and between α_2(20$\bar{2}$1) and α_2(20$\bar{2}\bar{1}$) are of 52.32° and 56.31°, respectively. These angles agree well with the observed ring shape between 50 and 70° taking into account the spread of the central peak of ± 11° and ± 9° parallel and perpendicular to the laser scan direction, respectively. This spread indicates a misalignment of the α_2 phase with the out-of-plane direction and is caused by slightly different crystal orientation depending on the position in the overlapping melt pools. Consequently, the ring shape of the α_2{20$\bar{2}$1} plane family is also spread. The different phase fractions of γ and α_2 in the two studied alloys have to be taken into account when interpreting the pole figure data for γ(111)/α_2(0002). In GE48-2-2 the resulting pole figure is dominated by the principal orientation of the γ phase as the main component. On the contrary, the pole figure of the same reflection for OX 45-3 ODS reflects the orientation of mainly α_2(0002), as only a minor fraction of γ is present in this alloy. The difference in data smoothness for the two alloys is explained by the different grain sizes of the formed microstructures. GE48-2-2 formed a very fine dendritic microstructure providing a multitude of different grains that simultaneously fulfill the diffraction conditions. The coarser structure in OX 45-3 ODS provides only a reduced number of grains that can contribute to diffracted intensity in a certain direction. Thus a speckle-like intensity distribution is observed in the pole figures of OX 45-3 ODS. However, these differences related to the dual phase microstructures of the alloys do not change the fact, that the overall degree of texture after DMD processing is significantly reduced in the β-solidifying OX 45-3 ODS alloy. As observed from the orientations of the lamellar colonies after annealing, there seems to be also no preferential lamellar orientation after thermal annealing (Fig. 7d and f).

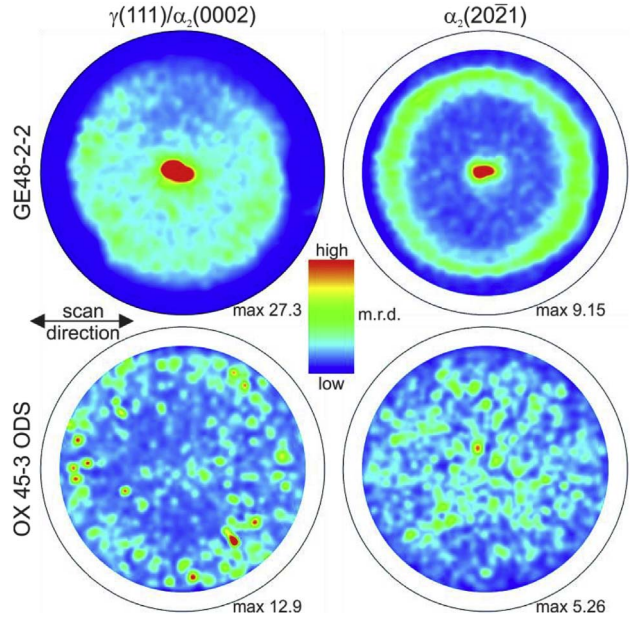

Fig. 9. XRD pole figures of DMD processed GE48-2-2 (top) and OX 45-3 ODS (bottom) for the most intense reflections γ(111)/α_2(0002) (left) and α_2(20$\bar{2}$1) (right). The coloring corresponds to low (blue) to high (red) values of m.r.d. The laser scan direction is horizontal for all subfigures. The part top surface normal is out-of-plane and in the center of the pole figures. (For interpretation of the references to colour in this figure legend, the reader is referred to the web version of this article.)

The results clearly show the possibility to consolidate OX 45-3 ODS using DMD. Furthermore, the chosen β-solidifying alloy induces significantly reduced texture in as-processed parts. Finally, the obtained microstructure can be transformed to a conventionally applied one by adapted thermal annealing (see Section 4.2). The compatibility of the developed ODS alloy with DMD opens possibilities to produce larger complex shaped ODS TiAl components which cannot be efficiently produced by powder-bed based methods as SLM or have too intricate features to be just produced by solid state sintering. Furthermore, the geometrical freedom in DMD processing facilitates controlled preheating to avoid the formation of large residual stresses, part deformation and potentially cracking.

4.4. ODS particle incorporation

It was shown that the OX 45-3 ODS alloy can be consolidated using solid state and additive liquid state processing technologies. In ODS alloys, the size and distribution of the ODS particles is crucial for the desired properties. Based on the well-known Orowan-relation

$$\sigma_{or} = M\frac{Gb}{2(l-r)} \tag{6}$$

where M = 3 is the conversion factor between shear and normal stress, G is the shear modulus, b is the Burgers vector, the stress σ_{or} is increased with smaller particle diameter r and smaller inter-particle distance l for non-cuttable particles. For dispersion strengthened ordered intermetallics more complex models are applied in order to account for detachment of the dissociated dislocations from the embedded particles [25]. The optimum dispersoid diameter d is then related to the dissociation width w by $w/d \approx 0.6$. As the involved energies of the formed

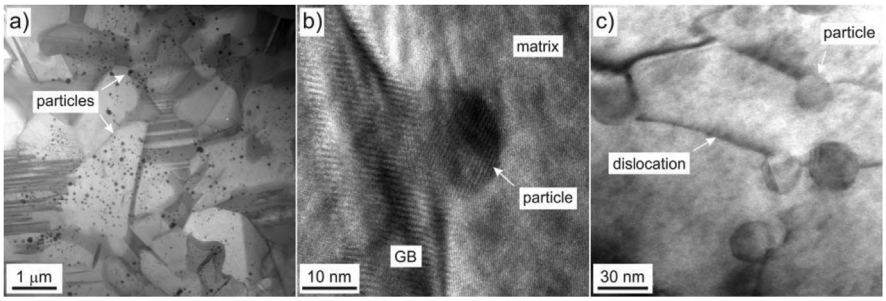

Fig. 10. Microstructure of SPS OX 45-3 ODS stabilized at 1123 K for 12 h a) STEM bright-field micrograph showing the distribution of fine ODS particles, b) HRTEM micrograph of an ODS particle pinning a grain boundary (GB) in the intermetallic matrix, c) TEM micrograph of ODS particles interacting with dislocations.

faults in TiAl alloys are comparably high, the corresponding dislocation dissociation width is typically less than 8 nm [26]. Consequently, the most effective dispersoid size for enhanced creep strength in ODS TiAl alloys is around 13 nm or less. For the dissociated super-dislocations the slightly larger particles are more effective while ordinary dislocations are more effectively hindered in their movement by smaller dispersoids. Fig. 10a shows the distribution of fine dispersoids throughout the intermetallic matrix in SPS OX 45-3 ODS stabilized at 1123 K for 12 h. The median particle size and volume number density were determined as 29 nm and $4.4{\cdot}10^{20}$ m^{-3}. The calculated median particle interspacing is 134 nm. The dispersoids are present in the equiaxed grains as well as in the lamellar colonies. The obtained particle sizes are comparable to the particle sizes in recrystallized PM2000, an established ODS Fe-base alloy [14,27]. Already in the stabilized state, grain boundary pinning was observed (Fig. 10b). The particles stop grain boundary movement and effectively retain a fine microstructure and also seem to slow down the $\gamma \rightarrow \alpha$ phase transformation as discussed in section 4.1. It is observed, that the particles interact with dislocations in the material (Fig. 10c). Dislocation pinning at the particles and bowing in between is evident. During service at elevated temperature these effects can be exploited to retain a desired microstructure - i.e. coarse grains for creep loading - for enhanced mechanical properties and long term stability. Fig. 11a shows the observed particle size distributions for solid state and additive liquid state processing. Fitted log-normal distribution curves are shown overlaid. Comparing these results it is evident, that liquid state processing leads to a certain degree of particle coarsening due to the high temperature and the presence of a liquid phase allowing fast diffusion of the elements necessary for particle growth. The diffusion of Y and O is limiting the growth of pure Y_2O_3 particles. The formation of higher-order oxides containing Ti and/or Al and having various crystal structures has been described earlier for Al-containing ODS alloys [27]. Specifically for TiAl alloys, the formation of Y-Al-O particles has been observed [19]. Consequently, the particle coarsening is not limited only by the diffusion of Y anymore and rapid growth can occur in the liquid state by incorporation of Ti and/or Al. After SPS and stabilization at 1123 K for 12 h a rather sharp size distribution with a median size of 29 nm is preserved. In SLM processed material a slightly broader distribution with a median size of 82 nm is observed. The volume number density is decreased to $7.4{\cdot}10^{18}$ m^{-3}. Consequently, the median particle interspacing is increased to 554 nm. DMD processing leads to a very broad size distribution ranging from sub-50 nm dispersoids to particles with a diameter of several hundreds of nanometers. These large particles are recognizable due to their high Y-content in BSE SEM micrographs (Fig. 7d). In accordance with the coarsening also the volume number density is reduced to $1.1{\cdot}10^{18}$ m^{-3}. The calculated median particle interspacing becomes relatively large with 1043 nm. Comparing the different consolidation methods, reducing the energy input in the material during processing clearly reduces the preserved oxide particle size. The two applied liquid state processing technologies SLM and DMD have greatly different heat input and melt pool sizes based on their laser spot diameters and area energy densities of 100 µm and 1.3 mm, and 4.5 J/mm^2 and 120 J/mm^2, respectively. Fig. 11b shows the correlation of oxide particle size

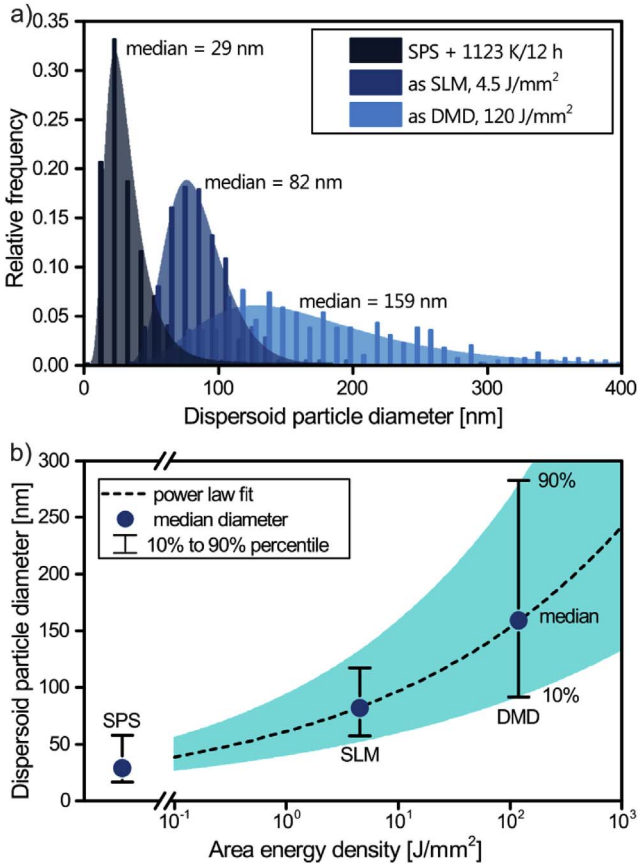

Fig. 11. a) Size distribution of ODS particles in solid state SPS sintered and stabilized, SLM and DMD processed OX 45-3 ODS. Least-square-fitted log-normal distribution curves are shown overlaid as well as the corresponding median value. b) Correlation of median ODS particle diameter and area energy in laser processing. The value for SPS sintered material is shown for comparison. A power law fit and the estimated 10%–90% percentile range are shown overlaid.

distribution and applied area energy density. The results from solid state SPS are shown for comparison. Overlaid is a power law fit of the median particle size according to

$$d = a{\cdot}E_a^{\frac{1}{m}} \tag{7}$$

where d is the median oxide particle diameter, a is the proportionality constant, E_a is the area energy density and m is the growth exponent. Simulations on melt pool life times in SLM show an approximately linear dependence on applied area energy density [28] (Supplementary Fig. S2). This allows applying a conventional parabolic diffusion-dominated growth model with $d \sim t^{\frac{1}{m}}$ where $t \sim E_a$ is the time and linear proportional to the area energy density E_a. The data and the fitted curve indicate that the energy input would need to be decreased to very low and finally unreasonable values to obtain similar particle sizes by liquid state processing as in solid state SPS material. It also

Table 2
Vickers hardness (HV ± 1σ) of SPS and DMD consolidated ODS-containing OX 45-3 ODS and ODS-free OX 45-3 and DMD consolidated GE48-2-2.

Process and Material	Condition	HV ± 1σ
SPS OX 45-3	1123 K/12 h	441 ± 29
	1673 K/15 min + 1123 K/12 h	409 ± 26
SPS OX 45-3 ODS	as SPS	505 ± 18
	1123 K/12 h	477 ± 16
	1573 K/15 min + 1123 K/12 h	471 ± 23
	1673 K/15 min + 1123 K/12 h	485 ± 15
DMD OX 45-3 ODS	as DMD	564 ± 61
	1123 K/12 h	546 ± 38
	1573 K/15 min + 1123 K/12 h	469 ± 25
DMD GE48-2-2	as DMD	512 ± 45
	1123 K/12 h	410 ± 19
	1573 K/15 min + 1123 K/12 h	358 ± 15

shows the limited effect of slight parameter variations in process control, as area energy input between SLM and DMD in this work differs by a factor of ~27, while the median dispersoid size is only increased by a factor of 2. However, if liquid state AM technologies based on very fine focused beams at low power and high scanning speeds are applied, particle sizes comparable to SPS seem to be possible. Generally, the life time of the melt pool needs to be minimized to yield the smallest particles.

The retained fraction of dispersoids after SLM and DMD processing is decreased to 38% and 41%, respectively, compared to SPS material. Slagging-off due to relatively low scanning speeds and slow solidification in DMD explains the observed losses and is confirmed by Y_2O_3 forming on the surface. Generally, a reduction of particles after SLM and DMD processing can be explained by a combination of slagging-off, dissolution and potentially also formation of dispersoids below the detection limit. No Y_2O_3 was observed on the surface of SLM processed material, indicating that the latter two processes play a dominant role. Future work will be dedicated to study the dispersoid size, stability and composition after processing.

4.5. Hardness of consolidated material

The hardness of SPS and DMD consolidated material was measured to analyze the effects of ODS incorporation and different consolidation methods on the mechanical properties (Table 2). Comparing the ODS-containing and ODS-free SPS consolidated alloy a beneficial effect of the yttria addition is evident. After a stabilization annealing at 1123 K for 12 h the ODS-free variant has 441 ± 29 HV, while OX 45-3 ODS has 477 ± 16 HV. This difference gets accentuated after high temperature annealing at 1673 K. The hardness of OX 45-3 is reduced to 409 ± 26 HV, while it is increased in OX 45-3 ODS to 485 ± 15 HV. DMD processed material has a high hardness in the as-processed state due to a high fraction of α_2 (Figs. 7 and 8) After thermal annealing at 1123 K for 12 h the hardness is slightly reduced to 546 ± 38 HV but still significantly higher than for SPS material annealed similarly. After high temperature annealing at 1573 K for 15 min and 1123 K for 12 h, similar hardness values are obtained for SPS and DMD processed OX 45-3 ODS, 471 ± 23 and 469 ± 25 HV, respectively. The DMD processed GE48-2-2 material shows lower hardness after processing and after all thermal annealing compared to OX 45-3 ODS. The similarity of hardness of annealed SPS and DMD material has extensive implications, as the microstructure of SPS and DMD material is different. In SPS material a fine duplex microstructure is observed, while DMD produces first a columnar structure of mainly α_2 that decomposes into a near-lamellar microstructure during thermal annealing (Figs. 4 and 7). Naturally, the finer SPS structure would be expected to provide the higher hardness due to a strength increase according to a Hall-Petch relation. Such behavior is observed when comparing SPS consolidated OX 45-3 and OX 45-3 ODS. The high hardness of DMD processed material indicates that the size of the lamellar colonies is not the factor determining increased hardness. Although the effect can be attributed to the introduction of the dispersoids, it remains unclear if it is only the presence of the particles or if the dispersoids are partly dissolved in the melt leading to a doping effect of the matrix. Given the reactivity of TiAl alloy melts and the associated problems of finding suitable ceramics for crucibles such a mechanism has to be considered. Despite the hardness cannot be directly used as a measure for the mechanical performance of TiAl alloys, the measurements indicate that the mechanical properties in OX 45-3 ODS are increased by the introduction of Y-based dispersoids. These effects are also observed after liquid phase AM processing by DMD. A more detailed study of the mechanical properties of the consolidated ODS material will be reported in a separate paper.

5. Summary and conclusions

- SPS OX 45-3 ODS has superior microstructural stability up to 1573 K compared to the ODS-free variant. The median particle size is 29 nm at a volume number density of $4.4{\cdot}10^{20}$ m^{-3}.
- SLM produces a coarse grained α_2-rich microstructure with a median dispersoid size of 82 nm at a volume number density of $7.4{\cdot}10^{18}$ m^{-3}. Upon annealing at 1123 K for 12 h, microstructural refinement into fine lamellar material is demonstrated. The retained fraction of dispersoids is 38% compared to SPS material.
- After DMD also a coarse grained α_2-rich microstructure is formed. Fine grained material is obtained after heat treatment at 1123 K for 12 h. Coarse grained material for enhanced creep resistance is observed after a two-step heat treatment at 1573 K/15 min + 1123 K/12 h. Incorporated particles have a median size of 159 nm at a number density of $1.1{\cdot}10^{18}$ m^{-3}. The as processed material shows significantly reduced texture and more evenly distributed intensity for the measured $\gamma(111)/\alpha_2(0002)$ and $\alpha_2(2021)$ reflections compared to DMD GE 48-2-2 alloy (Ti-48Al-2Cr-2Nb). The retained fraction of dispersoids is 41% compared to SPS material.
- Hardness measurements show superior values for SPS OX 45-3 ODS compared to its non-ODS counterpart.

From the obtained results it can be concluded that ODS TiAl alloys can be successfully produced by mechanical alloying and be consolidated by SPS, SLM and DMD. Especially the incorporation of small oxide particles using liquid state AM processing based on rapid solidification is a novel approach in TiAl alloys and was here reported for the first time according to the authors' knowledge. The compatibility of the developed Ti-45Al-3Nb ODS alloy with different processing technologies is foreseen to allow the use of solid state sintering and liquid state AM technologies to produce complex components using multi-step manufacturing taking advantage of the individual processing characteristics. The same alloy can then be used for a geometrically simple, sintered support structure with smaller oxides, combined with highly complex features produced by AM on top containing larger particles.

Acknowledgement

The authors thank H.-R. Elsener for conducting the high-vacuum annealing, A. Lis for the hardness measurements and S. Populoh and R. Widmer for SPS consolidation. The research leading to these results has received funding from the European Union Seventh Framework Program [FP7/2007–2013] under grant agreement no. 310279 (OXIGEN).

Appendix A. Supplementary data

Supplementary data related to this article can be found at http://dx.doi.org/10.1016/j.intermet.2017.07.004.

References

[1] Y.-W. Kim, Ordered intermetallic alloys, Part III: gamma titanium aluminides, JOM 46 (1994) 30–39.

[2] H. Clemens, S. Mayer, Design, processing, microstructure, properties, and applications of advanced intermetallic TiAl alloys, Adv. Eng. Mater 15 (2013) 191–215.

[3] L. Löber, F.P. Schimansky, U. Kühn, F. Pyczak, J. Eckert, Selective laser melting of a beta-solidifying TNM-B1 titanium aluminide alloy, J. Mater. Process. Technol. 214 (2014) 1852–1860, http://dx.doi.org/10.1016/j.jmatprotec.2014.04.002.

[4] J. Gussone, Y.-C. Hagedorn, H. Gherekhloo, G. Kasperovich, T. Merzouk, J. Hausmann, Microstructure of γ-titanium aluminide processed by selective laser melting at elevated temperatures, Intermetallics 66 (2015) 133–140, http://dx.doi.org/10.1016/j.intermet.2015.07.005.

[5] T. Vilaro, V. Kottman-Rexerodt, M. Thomas, C. Colin, P. Bertrand, L. Thivillon, S. Abed, V. Ji, P. Aubry, P. Peyre, T. Malot, Direct fabrication of a Ti-47Al-2Cr-2Nb alloy by selective laser melting and direct metal deposition processes, Adv. Mater. Res. 89–91 (2010) 586–591.

[6] S. Franzen, B. Karlsson, R. Dehoff, U. Ackelid, O. Rios, C. Parish, W. Peters, Microstructural properties of gamma titanium aluminide manufactured by electron beam melting, Min. Met. Mater. Soc. (2011) 455–462.

[7] J. Schwerdtfeger, C. Körner, Selective electron beam melting of Ti-48Al-2Nb-2Cr: microstructure and aluminium loss, Intermetallics 49 (2014) 29–35.

[8] L.E. Murr, S.M. Gaytan, A. Ceylan, E. Martinez, J.L. Martinez, Characterization of titanium aluminide alloy components fabricated by additive manufacturing using electron beam melting, Acta Mater 58 (2010) 1887–1894.

[9] W. Liu, J.N. Dupont, Fabrication of carbide-particle-reinforced titanium aluminide-matrix composites by laser-engineered net shaping, Metall. Mater. Trans. A 35 (2004) 1133–1140.

[10] D. Srivastava, I.T.H. Chang, M.H. Loretto, The effect of process parameters and heat treatment on the microstructure of direct laser fabricated TiAl alloy samples, Intermetallics 9 (2001) 1003–1013.

[11] C. Kenel, C. Leinenbach, Influence of cooling rate on microstructure formation during rapid solidification of binary TiAl alloys, J. Alloys Compd. 637 (2015) 242–247, http://dx.doi.org/10.1016/j.jallcom.2015.03.016.

[12] C. Kenel, C. Leinenbach, Influence of Nb and Mo on microstructure formation of rapidly solidified ternary Ti-Al-(Nb, Mo) alloys, Intermetallics 69 (2016) 82–89, http://dx.doi.org/10.1016/j.intermet.2015.10.018.

[13] C. Kenel, D. Grolimund, J.F. Fife, V.A. Samson, H. Van Swygenhoven, C. Leinenbach, Combined in situ synchrotron microXRD and high-speed imaging on rapidly heated and solidified Ti-48Al under additive manufacturing conditions, Scr. Mater. 114 (2016) 117–120.

[14] T. Boegelein, S.N. Dryepondt, A. Pandey, K. Dawson, G.J. Tatlock, Mechanical response and deformation mechanisms of ferritic oxide dispersion strengthened steel structures produced by selective laser melting, Acta Mater 87 (2015) 201–215, http://dx.doi.org/10.1016/j.actamat.2014.12.047.

[15] G. Molénat, M. Thomas, J. Galy, A. Couret, Application of spark plasma sintering to titanium aluminide alloys, Adv. Eng. Mater 9 (2007) 667–669.

[16] T. Voisin, J.-P. Monchoux, L. Durand, N. Karnatak, M. Thomas, A. Couret, An innovative way to produce γ-TiAl blades: spark plasma sintering, Adv. Eng. Mater 17 (2015) 1408–1413, http://dx.doi.org/10.1002/adem.201500019.

[17] D.S. Schwartz, P. Fraundorf, S.M.L. Sastry, TEM study of B- and Er-containing dispersoids in rapidly solidified dispersion-strengthened titanium aluminde alloys, Ultramicroscopy 37 (1991) 310–317.

[18] C. Suryanarayana, F.H. Froes, Mechanical alloying of titanium-base alloys, Adv. Mater 5 (1993) 96–106.

[19] P.B. Trivedi, E.G. Baburaj, A. Genc, L. Ovecoglu, S.N. Patankar, F.H. Froes, Grain-size control in Ti-48Al-2Cr-2Nb with yttrium additions, Metall. Mater. Trans. A 33A (2002) 2729–2736.

[20] H. Clemens, W. Wallgram, S. Kremmer, V. Güther, A. Otto, A. Bartels, Design of novel β-solidifying TiAl alloys with adjustable β/B2-phase fraction and excellent hot-workability, Adv. Eng. Mater 10 (2008) 707–713.

[21] J.O. Andersson, T. Helander, L. Höglund, P.F. Shi, B. Sundman, Thermo-Calc, DICTRA, Computational tools for materials science, Calphad 26 (2002) 273–312.

[22] V.T. Witusiewicz, A.A. Bondar, U. Hecht, T.Y. Velikanova, The Al-B-Nb-Ti system IV. Experimental study and thermodynamic re-evaluation of the binary Al-Nb and ternary Al-Nb-Ti systems, J. Alloys Compd. 472 (2009) 133–161.

[23] F. Appel, J.D.H. Paul, M. Oehring (Eds.), Gamma Titanium Aluminide Alloys, Wiley-VCH, 2011.

[24] J. Zollinger, V. Witusiewicz, A. Drevermann, D. Daloz, U. Hecht, Solidification of high Nb containing TiAl based alloys, Int. J. Cast. Met. Res. 22 (2009) 339–342, http://dx.doi.org/10.1179/136404609X368163.

[25] E. Arzt, E. Göhring, A model for dispersion strengthening of ordered intermetallics at high temperatures, Acta Mater 46 (1998) 6575–6584.

[26] S.H. Whang, D.P. Pope, C.T. Liu, High temperature aluminides and intermetallics, Proceedings of the Second International ASM Conference on High Temperature Aluminides and Intermetallics, September 16-19, 1991, Elsevier, San Diego, CA, USA, 2013.

[27] C. Capdevila, G. Pimentel, M.M. Aranda, R. Rementeria, K. Dawson, E. Urones-Garrote, G.J. Tatlock, M.K. Miller, Role of Y-Al oxides during extended recovery process of a ferritic ODS alloy, JOM 67 (2015) 2208–2215, http://dx.doi.org/10.1007/s11837-015-1559-5.

[28] Y. Li, D. Gu, Parametric analysis of thermal behavior during selective laser melting additive manufacturing of aluminum alloy powder, Mater. Des. 63 (2014) 856–867, http://dx.doi.org/10.1016/j.matdes.2014.07.006.